PROCEEDINGS, 50th Workshop on Geothermal Reservoir Engineering
Stanford University, Stanford, California, February 10-12, 2025
SGP-TR-229

Rough Fracture Characterization in Enhanced Geothermal Systems (EGS): Numerical Simulation Updates

Sarah Sausan, Roland Horne

Dept. of Energy Science and Engineering, Stanford University

sausan@stanford.edu, horne@stanford.edu

Keywords: rough fracture, EGS, numerical simulation, roughness, CFD, Navier-Stokes

ABSTRACT

The artificial fractures in EGS are created within the context of natural factors such as geology, geomechanics, and geochemistry, as well as engineering techniques used during stimulation, such as the use of proppant and acids. Fracture characterization, i.e., gathering information regarding fractures' physical properties, such as aperture, hydraulic conductivity, and network distribution patterns, provides the source of information for modeling and engineering the subsurface reservoir appropriately.

At the near-wellbore scale, the fracture planes around the well are examined to provide an understanding of the feed zone behavior. At the EGS Collab site, it was observed that during a downhole camera survey of a flowing wellbore the inflow pattern from the producing fractures was not sheet-like but rather composed of sporadic point sources. This observation can be explained by considering that fracture surfaces are rough; preferential fluid flow pathways emerged across a fracture plane due to its roughness.

To simulate the fluid flow behavior between the crevices of rough fracture, a displacement discontinuity model (DDM) was used to represent rough fracture faces under varying stress regimes. Then, the geometry of the fracture space was built into a three-dimensional model to simulate the fluid flow and heat transfer across the fracture planes using a Computational Fluid Dynamics (CFD) simulator.

The rough fracture modeling in this study could successfully model the fluid flow for a roughness distribution corresponding to a shear stress and normal stress combination of -6MPa and 6MPa, respectively. As the stress regimes heavily influence the aperture distribution, subsequent scenarios were modeled across parametric simulation involving a range of shear and normal stress and compared with the reference. Radial flow behavior for each stress regime was simulated to investigate the roughness relationship with varying stress regimes.

1. INTRODUCTION

The artificial fractures in EGS are created within the context of natural factors such as geology, geomechanics, and geochemistry, which determine the fractures' shape, size, orientation, interaction with pre-existing natural fractures, and other physical properties. Furthermore, engineering techniques used during stimulation, may further modify the fracture properties. As much as we may strive to create the ideal fractures on the first attempt, the reality is that productive fractures are achieved through a learning process, where fracture characteristics are continuously inferred and evaluated to inform subsequent measures that can capitalize on or address the observed fracture properties.

Therefore, fracture characterization, i.e., gathering information regarding fractures' physical properties, such as aperture, hydraulic conductivity, and network distribution patterns, is crucial to perform throughout the lifetime of an EGS site. Characterization provides the source of information for modeling and engineering the subsurface reservoir appropriately. Fracture characterizations encompass various techniques across multiple spatial and temporal scales.

At the wellbore scale, fracture characterization focuses on understanding the feed zones and analyzing inflow rates/patterns and thermal energy (enthalpy and temperature), along with its position, aperture size, and other associated properties. At the near-wellbore scale, the fracture planes around the well are examined to provide an understanding of the feed zone behavior. For instance, it was observed at the EGS Collab site that during a downhole camera survey of a flowing wellbore (Fu et al., 2019; Fu and Morris, 2020) shown in Figure 1, the inflow pattern from the producing fractures was not sheet-like but rather composed of sporadic point sources. Modeling the fracture planes and connecting them to the observed wellbore-scale data would help explain this phenomenon.

Thus, the fluid flow behavior at rough fractures was examined through numerical simulations. To investigate the observation that the inflow pattern from an EGS well's feed zone was not sheet-like but rather composed of sporadic point sources, we considered that fracture surfaces are rough, allowing preferential fluid flow pathways to emerge across a fracture plane. This paper highlights the results of the numerical simulation.

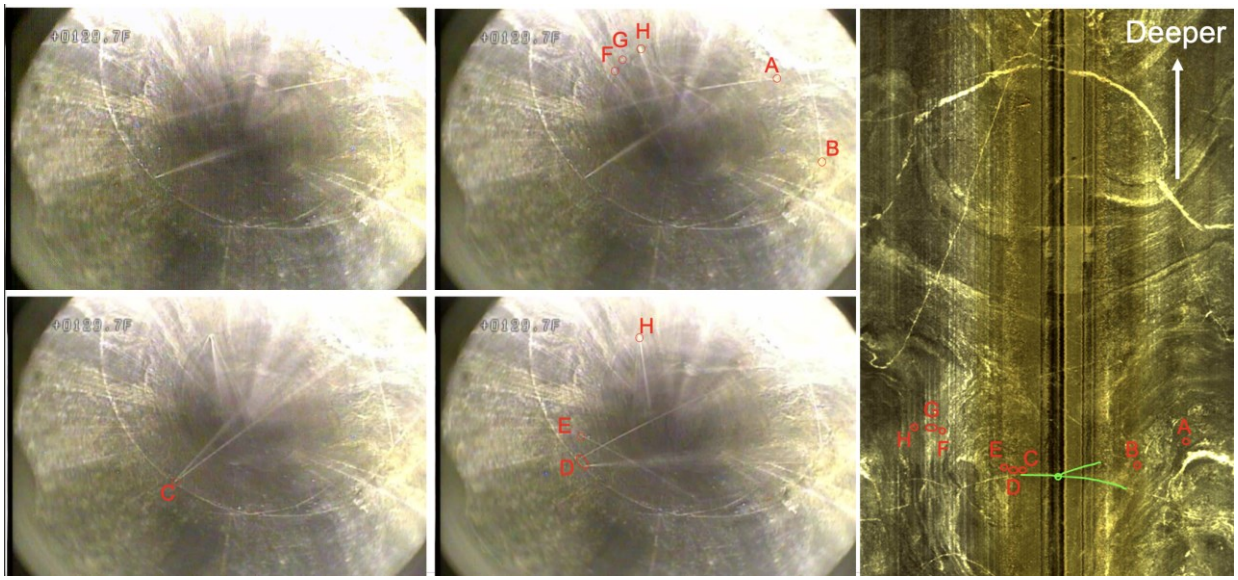

Figure 1: Jet locations at 129 ft depth of Well EP-1 observed by the downhole camera surveys and mapped against the corresponding image log. From Fu and Morris (2020).

2. ROUGH FRACTURES OVERVIEW

Fractures are often represented with a smooth parallel-plate model, thus assumed to have uniform hydraulic aperture and permeability. In reality, fracture walls are rough and uneven, thus disrupting the flow pathway into channels, cross-flows, back-flows, and eddy flows (Zou et al., 2017; Xiong et al., 2018). Laboratory experiments and flow simulations by Ishibashi et al. (2012) demonstrated that up to 70% of the fracture area does not facilitate flow (Figure 2a, b).

Field experiments by Abelin et al. (1988, 1991) have also confirmed the occurrence of flow channeling and disturbances within the same fracture plane due to its heterogeneity. For instance, a tracer experiment conducted in a granitic fracture at the Stripa mine in Sweden involved injecting five different tracers at 5 cm intervals along the wellbore on the same fracture plane. The results indicated significant flow channeling even over short distances of less than 2 m, with some tracers being entirely disconnected (Figure 2c).

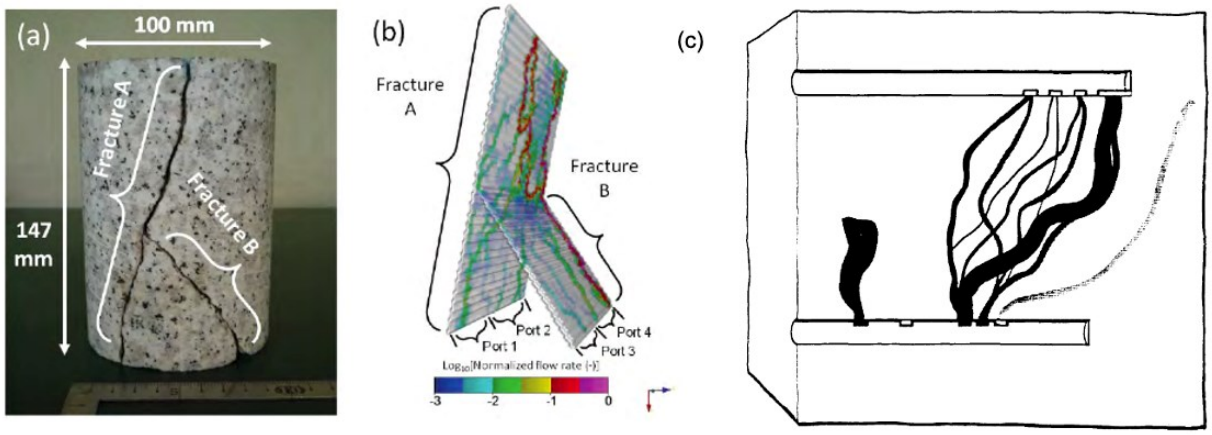

Figure 2: (a) Granite rock sample and (b) flow simulation onto the sample's fracture surfaces by Ishibashi et al. (2012) showed that only 30% of the fracture planes were conducive to flow; (b) tracer experiment at Stripa mine, Sweden by Abelin et al. (1988) demonstrated flow channeling within a granitic fracture plane due to its roughness.

The roughness of a fracture, also known as "asperity," can be quantified with a simple definition of asperity height Z, which is the difference between the maximum and minimum asperity height (Chen et al., 2015). More sophisticated quantification of roughness includes calculating the root mean square value of the profile RMS (Tse and Cruden, 1979) or the skewness S_{sk} and kurtosis coefficient R_{ku}; (Thomas, 1981). Matedness of a rough fracture refers to the extent to which the fracture surfaces match or interlock. Fracture surfaces

are considered mated when the correlation occurs only on a large scale and unmated when they do not correlate on both small and large scales (Brown and Scholz, 1986).

The roughness of a fracture determines the aperture distribution, which in turn controls the fluid flow pathways. Fluid primarily flows through the effective aperture (or hydraulic aperture) portion of the mechanical aperture (Xiao et al., 2021). The size of the hydraulic aperture depends on dynamic properties such as dynamic viscosity, flow rate, and pressure differentials between the inlet and outlet as governed by Darcy's Law (Deng et al., 2013).

The stress regime in which the rough fractures formed and the changes in stress regimes over geological history play an important role in determining the roughness pattern and subsequent flow pathways. Zhang and Chai (2020) consolidated the relationship between roughness and permeability under increasing normal stress in unmated fractures through a review of published experimental and numerical results, as follows:

- **Stage 1**: when normal stress is lower than a lower critical value (denoted as σA), rougher fractures tend to exhibit lower permeability.
- **Stage 2**: when normal stress exceeds σA but less than an upper critical value (denoted as σB), Rougher fractures exhibit larger permeability.
- **Stage 3**: when normal stress exceeds σB, the effect of roughness on permeability is no longer consequential, and the fractures with different roughness tend to exhibit a similar permeability.

Shear stresses cause the rock surfaces to slip and slide along the fracture walls, altering their roughness and contact properties. Abrasion and microcracks are often formed, creating additional roughness that may obstruct the flow paths and counter the effects of shear dilation (Javadi et al., 2014). The obstruction is especially more severe when infill materials like weathering and hydrothermal veins are present (Lee et al. 2015). Shear stress also often results in nonlinear flow behavior; this phenomenon is known as shear-induced flow anisotropy and is well-documented in fluid flow and solute transport. In rough fractures, this anisotropy is particularly pronounced (Amadei and Illangsekare, 1992; Auradou et al., 2005).

The mineral composition of the fractured rock and its infill materials influence roughness change under stress. Fang et al. (2017) demonstrated that roughness in strong-brittle rocks can result in larger permeability compared to weak-ductile rocks. In EGS, infill materials can be introduced artificially using proppants, such as sand, to prop open the fractures. When the effective pressure increases, permeability reduction in unfilled fractures significantly exceeds that in filled fractures, leading to elastic and inelastic deformations for the unfilled fractures and only inelastic compaction for the filled fractures (Wang et al., 2016). Coarser infill materials promote fluid flow; however, grain sizes that are too large can cause materials to settle by the fracture walls (Liu and Sharma, 2005).

3. MODELING ROUGH FRACTURES

3.1. Techniques and Formulation

Modeling rough fractures typically begins with obtaining surface elevation or aperture data derived from laboratory experiments. This study used surface elevation data from Co et al. (2017), which were obtained from granite and sandstone core samples that were sheared in compression tests (Figure 3a). These maps were used as the basis for two-dimensional fracture plane geometry. Co et al. (2017) developed a numerical simulator using the displacement discontinuity boundary element method (DDM) with integrated complementarity. This simulator allows for remote shear and normal stresses to be applied to the fracture plane, which results in the generation of modeled aperture and slip maps. A rectangular cutout of the resulting aperture map was then created (Figure 3b). A minimum local aperture of 1 x 10^{-10} m was defined for elements that did not open.

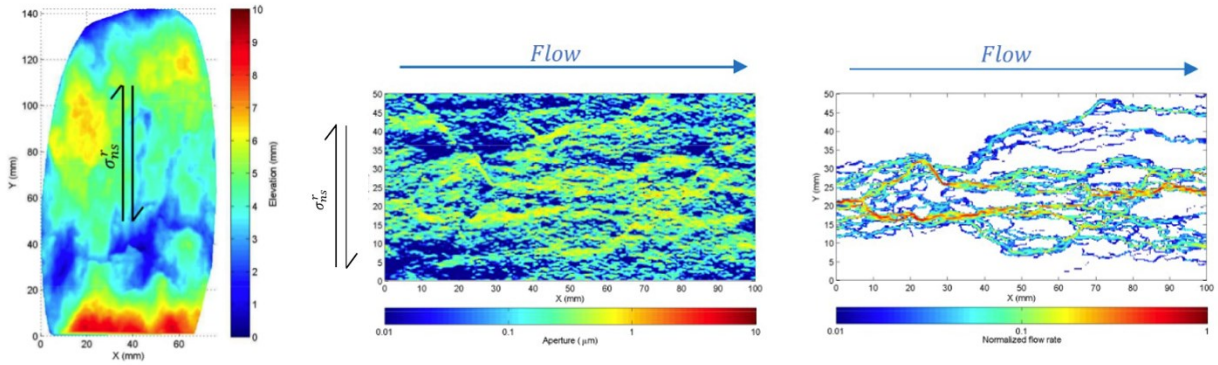

(a) Fracture elevation map

(b) Aperture map at σ_{shear} = 2 MPa and σ_{normal} = -1 MPa

(c) Normalized flow perpendicular to σ_{shear}

Figure 3: A sample of flow simulation on rough fracture modeling performed by Co et al. (2017).

Fluid flow simulations of rough fracture space often utilize the Cubic Law, as also used by Co et al. (2017). In their modeling, the simple Cubic Law permeability formula ((i.e., $k = b^2/12$) was used to convert aperture values into permeability. The permeability map was then set as input into a flow simulation program based on a finite value model. The simulation was conducted at steady state with single-phase flow and a grid block size of 0.25 mm x 0.25 mm. No-flow boundary conditions were applied to one pair of opposite rectangular sides, while the other pair had constant pressure boundary conditions set at 4000 psi and 2000 psi. The resulting pressure distribution was used to calculate flow rates using the cubic law expressions of linear flow, as shown in Equation ((**1**). A flow distribution map was then created to show the relative flow rate of areas with a flow rate value of at least one percent of the maximum flow rate (Figure 3c).

$$Q = \frac{b^3}{12}\left[\frac{W}{L}\right]\frac{1}{\mu}\Delta p \tag{1}$$

The Cubic Law is derived from approximating the incompressible Navier-Stokes equation, making simplified assumptions that can lead to underestimating or overestimating the flow rate. To accurately account for the complex fracture geometries and inertial terms, the full Navier-Stokes equation can be used to simulate flow in three-dimensional fractures. The rough fracture modeling in this study integrated the versatility of simulating aperture distribution using DDM with the improved accuracy of fluid flow simulation utilizing full Navier-Stokes equations in a three-dimensional fracture space.

Fluid flow in rough fractures is governed by the Navier-Stokes (NS) equation as shown in Equation (2):

$$\frac{\partial \mathbf{u}}{\partial t} + (\mathbf{u}\cdot\nabla)\mathbf{u} = \mathbf{F} - \frac{1}{\rho}\nabla p + \frac{\mu}{\rho}\nabla^2\mathbf{u} \tag{2}$$

This Navier-Stokes equation can be further simplified according to the modeling setup. For incompressible fluid like water, conservation of mass corresponds to conservation in volume $\nabla \cdot \mathbf{u} = 0$. Furthermore, simulation is performed at a steady state, thus ignoring the time derivative. Then, the equation $P = p + \rho g h$ can further simplify the Navier-Stokes form to:

$$\rho(\mathbf{u}\cdot\nabla)\mathbf{u} = \mu\nabla^2\mathbf{u} - \nabla P \tag{3}$$

where the left-hand side denotes inertial forces, and the first term on the right-hand side indicates viscous forces. If the inertial term is negligible compared with the viscous term, then the Navier-Stokes equation can be linearized into the Stokes equation:

$$\mu\nabla^2\mathbf{u} - \nabla P = 0 \tag{4}$$

The equation can further be simplified into the Reynolds equation by assuming that viscous forces dominate inertial forces and that aperture variation is gradual:

$$\nabla(e^3\cdot\nabla P) = 0 \tag{5}$$

Finally, when assuming the fracture planes are two smooth parallel plates, the cubic law can be derived to infer permeability from aperture size (i.e., $k = b^2/12$).

3.2. Modeling setup

This research utilized the ANSYS computational Fluid Dynamics (CFD) simulator governed by the Navier-Stokes equation at steady state using incompressible fluid in three-dimensional space. Flow is set as turbulent with realizable k–ε as a viscous method. In the realizable k–ε model, the turbulent viscosity is calculated by using an improved method, as detailed by Shaheed et al. (2019). The exact transport equation of the fluctuating component vorticity is used to derive the dissipation rate equation. The realizable k–ε model is considered more accurate compared to the k–ε model in predicting the distribution of the dissipation rate of flat and round jets. Also, better prediction is provided by the realizable k–ε model for the boundary layer characteristics in a large pressure gradient, separated and recirculating flows.

The rough fracture geometry was generated from the discontinuity displacement model (DDM) developed by Co et al. (2017). As much as -6 MPa shear stress (NS-6MPa) and 6 MPa normal stress (NN+6MPa) were applied, remotely deforming the aperture distribution measured from a granite sample in two dimensions. A false minimum thickness must be applied to form a three-dimensional aperture plane. As a reference, the minimum thickness value used for a successful CFD modeling by Chen et al. (2021) was 10 μm, which is equal to the maximum aperture value of the NN+6MPa/NS-6MPa. To successfully create a mesh and simulate flow in this research, the rough fracture plane was scaled up by a factor of 1000. This approach ensures that the minimum thickness is maintained while increasing the aperture value proportionally.

The original aperture distribution and the resulting three-dimensional fracture plane from DDM are illustrated in Figure 4a and b, respectively; the latter subsequently cropped into the same rectangular dimension with graphics shown by Co et al. (2017). Attempts were made to mesh the cropped fracture plane with minimal modification. However, passing the mesh quality check was difficult, leading to divergence in the fluid simulation (Case groups 1 and 2 in Table 3.2). We then conducted subsequent parametric simulations to test potential solutions. One approach involved smoothing the asperity geometry to minimize geometric irregularities such as highly skewed or left-handed elements. This smoothing method proved effective in achieving convergence. The use of smoothing is based on the understanding that the hydraulic aperture is a curvaceous subset of the geometric aperture.

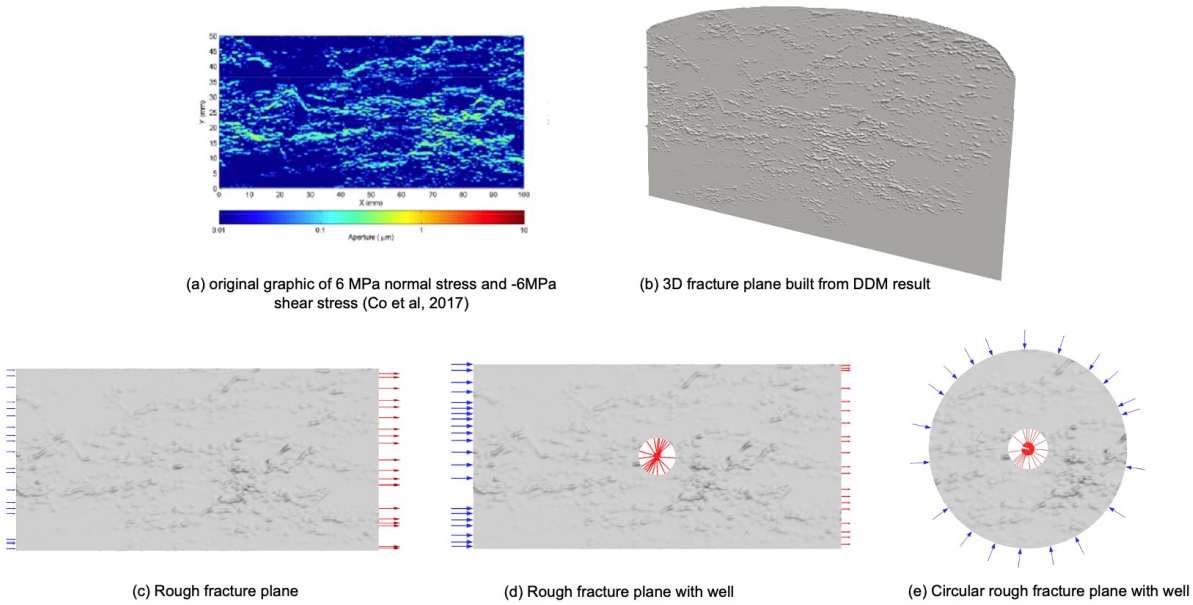

Figure 4: rough fracture plane geometry, meshing, and boundary conditions for numerical simulation

The successful mesh setup that could pass a volume mesh quality check for the skewness of less than 0.7 was achieved using polyhedral elements with sizes ranging from 1×10^{-5} to 2×10^{-4} m. Three different geometries were derived and are shown in Figure 4c, d, and e: the fracture plane, rough fracture plane with a well, and circular rough fracture plane with a well, respectively. The latter simulates radial flow and the closest setup, resembling the downhole camera survey observation at the EGS Collab project.

The boundary condition for the fluid flow simulation involves a pair of inlet and outlet (the blue and red arrows in Figure 4c and d) at opposing sides of the rectangle. Additionally, some scenarios place a well cutout as an additional outlet boundary (Figure 4d and e). Parametric scenarios were tested and summarized in Table 1. Each case group contains 1-5 cases. Corresponding simple fracture cases without roughness were also run and compared; the thickness follows the mean aperture value of the rough fracture surface, which is 0.027 mm.

Table 1: Parametric scenarios tested for rough fracture modeling

Case Group	Geometry	Parameter range	Converged?
1&2	Rough fracture plane	Comparing laminar vs turbulent viscous term (realizable k-epsilon). Also comparing the necessity of reverse flow prevention at the outlet. 100 psi pressure inlet, 0 psi pressure outlet.	No
3-1	Rough fracture plane, smoothed	Varying value of pressure inlet, pressure outlet, and fluid viscosity. Smaller element size by 1 order of magnitude compared to case group 1 & 2. Pressure inlet: 100 psi, 4000 psi Pressure outlet: 0 psi, 2000 psi Liquid H2O viscosity: 1e-3 Pa.s (standard) and 3e-4 Pa.s (used by Co et al. (2017))	Yes
3-2	Rough fracture plane, smoothed	Varying value of mass inlet with zero-pressure outlet. Mass inlet of 3.33e-1, 3.33e-2, and 3.33e-5 kg/s, corresponding to volumetric flow rate of 3.33e-4, 3.33e-5, and 3.33e-8 m^3/s in Chen et al. (2021)	Yes
4	Rough fracture plane, smoothed	Inlet and outlet at the top and bottom sides of the fracture plane (90deg rotation). Pressure-inlet: 4000 psi, pressure-outlet: 2000 psi	Yes

5-1	Simple fracture plane	Pressure-inlet: 4000 psi, pressure-outlet: 2000 psi	Yes
5-2	Simple fracture plane with well cutout *(r = 5 mm)*	Pressure-inlet: 4000 psi, pressure-outlet: 2000 psi	Yes
5-3	Circular simple fracture plane with *(r_{plane} = 5 mm)* with well cutout *(r_{well} = 5 mm)*	Pressure-inlet: 4000 psi, pressure-outlet: 2000 psi	Yes
6	Rough fracture plane, smoothed, with well cutout	Pressure-inlet: 4000 psi, pressure-outlet: 2000 psi	Yes
7	Circular fracture plane, smoothed, with well cutout	Pressure-inlet: 4000 psi, pressure-outlet: 2000 psi	Yes

4. RESULTS AND DISCUSSIONS

The base case of the simulation is reflected in Case 3-1d (Figure 5) where the pressure inlet is 4000 psi at the left boundary, and the pressure outlet is 2000 psi at the right boundary. These are the same boundary conditions as the comparable case from Co et al. (2017), which is considered as the reference. With the current meshing strategy, convergence could be reached fairly early at less than 150 iterations. Additionally, a simple fracture case was run.

The preferential fluid flow pathway is especially evident in the velocity magnitude map, sliced at around the midpoint between the mean value of the largest asperity to the fracture plane base (5×10^{-6} m) and the midpoint of the zero asperity to the plane base (1×10^{-6} m). Both show veining patterns comparable to the reference but with additional thin pathways. The reference employs the Cubic Law approach that is more simplified than the Navier-Stokes equation, and the difference in pattern reflects that. The preferential flow pattern coincides with intense turbulence. The roughness also influences the pressure distribution, with gradient change larger in areas with more flow. Also, as expected, the simple fracture case shows uniform distribution for pressure, velocity, and turbulence (amid some artifacts from meshing).

A 90-degree rotation of the inlet and outlet pair (Case 4-1a, Figure 6) is markedly different than the reference case, as convergence required more iterations, albeit stabilizing at around 900 iterations. The reference shows a flow pathway only near the left boundary, but the simulation shows a flow pattern dispersing in almost the entirety of the rough fracture plane. Furthermore, the geometric pattern of the left-to-right channel is still preserved in the simulation results, even with inlet-outlet direction rotations. The reference result of Case 4-1a seems constrained to the left side of the fracture and thus does not appear very convincing; therefore, this study's fluid flow simulation results are considered closer to representing real-world conditions.

A circular cutout in the middle of the fracture plane representing inflow to a wellbore (i.e., another pressure outlet) was put in Case 6-1 with boundary conditions kept the same as the base case 3-1d, shown in Figure 7. The well greatly influences and exacerbates the flow pathway; almost no flow passes to the right boundary. The circular rough fracture plane case (Case 7-1a, Figure 8) with well cutout is a more accurate representation of radial flow at near wellbore scale. The geometric channel in the left-right direction is still preserved, even with circular inlet boundary conditions. This finding indicates that the roughness pattern is very influential for the flow pathway, even for radial flow. The simple fracture case exhibits a uniform pressure, velocity, and turbulence intensity distribution with negligible fluctuations.

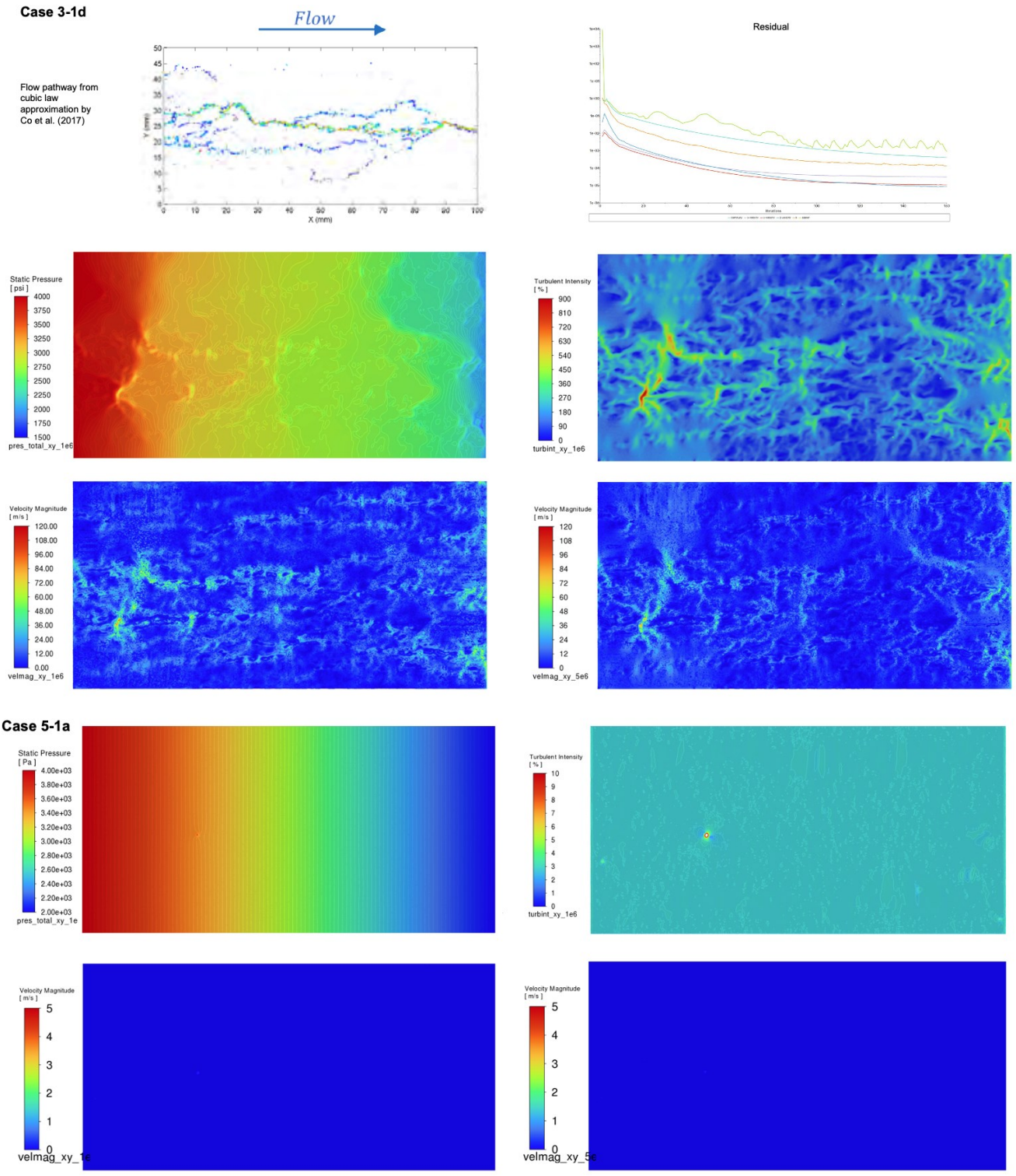

Figure 5: Simulation results for the base case 3-1d and simple fracture plane case 5-1a without roughness

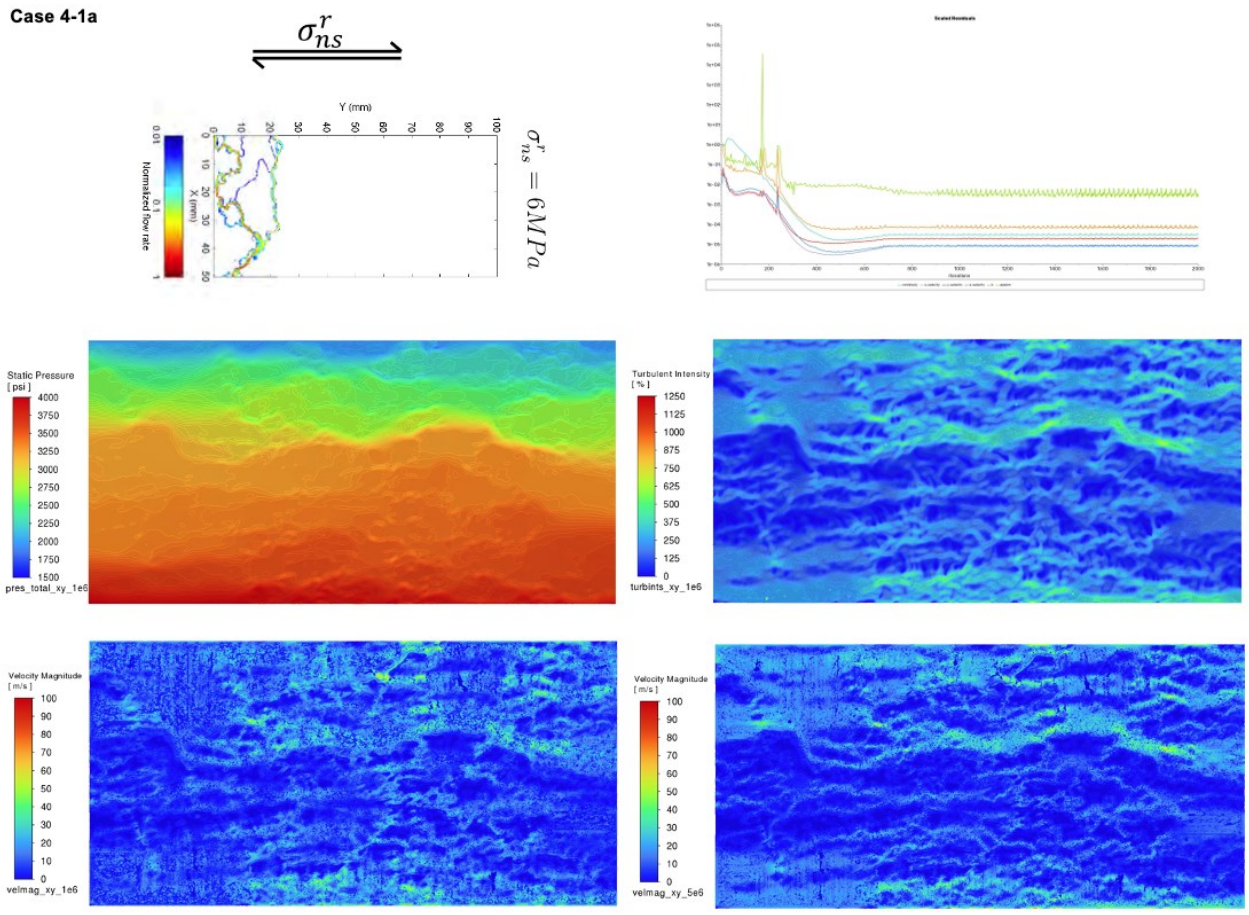

Figure 6: Simulation results for case 4-1a resembling the base case 3-1d but with 90deg rotation of inlet-outlet

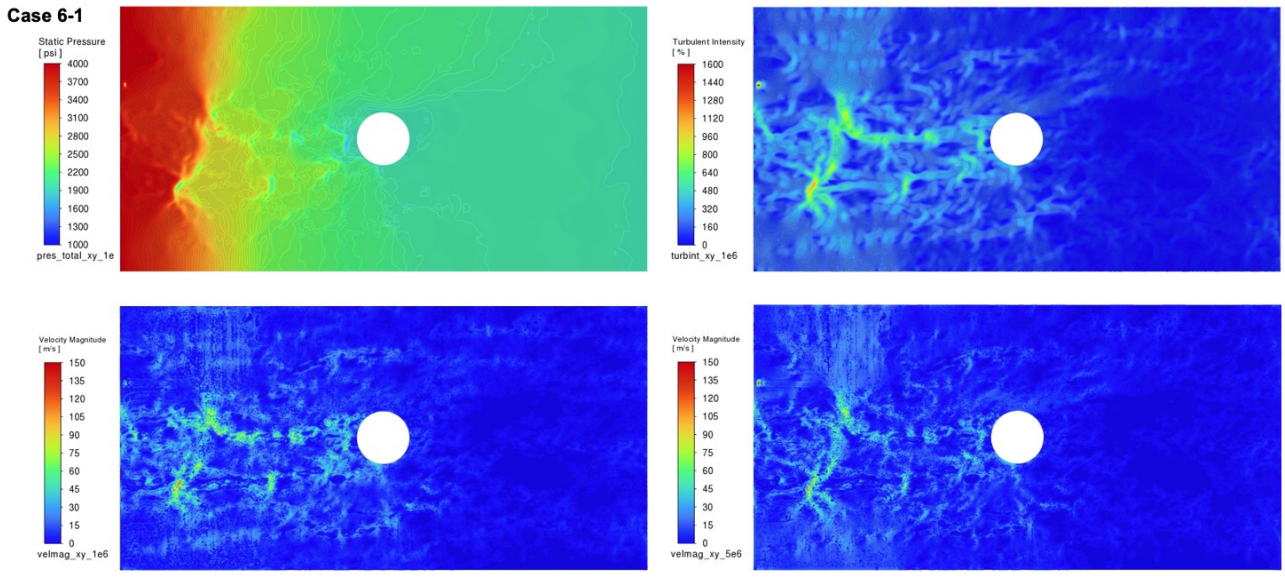

Figure 7: Simulation results for case 6-1 resembling the base case 3-1d but with a well-cutout radius of 5 mm.

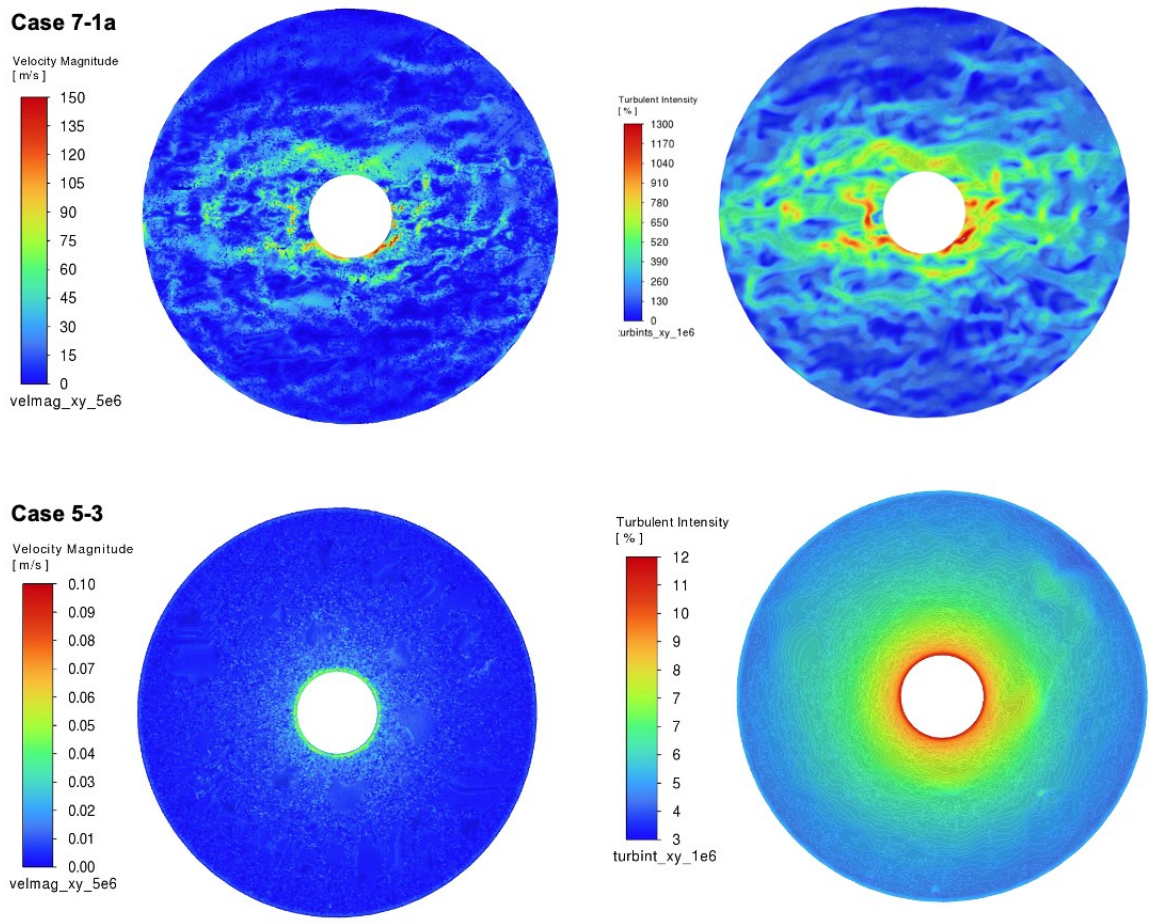

Figure 8: Simulation results for circular fracture plane with roughness (top) and without (bottom)

5. CONCLUSION AND FUTURE WORK

The rough fracture modeling so far could successfully represent the fluid flow for a roughness distribution corresponding to one shear stress/normal stress combination of -6MPa/6MPa, respectively. As the stress regimes heavily influence the aperture distribution, subsequent scenarios can be modeled across parametric simulation involving a range of shear and normal stress and compared with the reference. Radial flow behavior for each stress regime can be simulated to conclude the roughness relationship with varying stress regimes.

Geothermal systems are primarily governed by heat transfer, and thus, in addition to fluid flow, investigation regarding the relationship between roughness and heat transfer distribution is crucial. Okoroafor and Horne (2018) investigated heat transfer in anisotropic (i.e., rough) fracture using a finite-volume numerical simulator that still employs a cubic law model at a single-fracture EGS field setup. It would be interesting to extend the fluid flow modeling currently performed under the Navier-Stokes governing equation to include the energy equation, which can also model the heat transfer and resulting temperature distribution and compare that with the result from the reference. Moreover, heat transfer in radial flow can also be simulated.

Finally, the rough fracture model and the fluid flow and heat transfer simulation can be used to model tracer test data obtained in research concerning fracture characterization at the reservoir scale. This modeling will be able to bridge the rough fracture understanding at the near-wellbore scale to its importance in making sense of the fracture network and damage zones' influence on flow and heat transfer at the reservoir scale.

NOMENCLATURE

Symbol	Quantity	Unit
b, e	Aperture	mm
F	Body force	N/m^3
q	Volumetric flow rate	m^3/s
μ	Fluid dynamic viscosity	Pa·s
u	Flow velocity	m/s
L	Length of a rough rock fracture	m
ρ	Density	kg/m^3
k	Permeability	miliDarcy (mD)
ΔP	Pressure difference	Pascal; psi
∇P	Pressure gradient	Pa/m; psi/ft
t	Time	s
W	Width of a rough rock fracture	m

REFERENCES

Abelin H, Birgersson L, Ågren T, Neretnieks I (1988) A Channeling Experiment to Study Flow and Transport in Natural Fractures. MRS Proc 127:661. https://doi.org/10.1557/PROC-127-661

Abelin H, Birgersson L, Gidlund J, Neretnieks I (1991) A Large-Scale Flow and Tracer Experiment in Granite: 1. Experimental Design and Flow Distribution. Water Resources Research 27:3107–3117. https://doi.org/10.1029/91WR01405

Amadei R, Illangsekare T (1992) Analytical Solutions for Steady and Transient Flow in Non-homogeneous and Anisotropic Rock Joints. Int J Rock Mech Min Sci & Geomeeh 29:561–572

Auradou H, Drazer G, Hulin JP, Koplik J (2005) Permeability anisotropy induced by the shear displacement of rough fracture walls. Water Resources Research 41:2005WR003938. https://doi.org/10.1029/2005WR003938

Brown SR, Scholz CH (1986) closure of rock joints. J Geophys Res 91:4939–4948. https://doi.org/10.1029/JB091iB05p04939

Chen Y, Selvadurai APS, Zhao Z (2021) Modeling of flow characteristics in 3D rough rock fracture with geometry changes under confining stresses. Computers and Geotechnics 130:103910. https://doi.org/10.1016/j.compgeo.2020.103910

Chen Y-F, Zhou J-Q, Hu S-H, et al (2015) Evaluation of Forchheimer equation coefficients for non-Darcy flow in deformable rough-walled fractures. Journal of Hydrology 529:993–1006. https://doi.org/10.1016/j.jhydrol.2015.09.021

Co C, Pollard D, Horne R (2017) Towards a Better Understanding of the Impact of Fracture Roughness on Permeability-Stress Relationships Using First Principles. Proceedings, 42nd Workshop on Geothermal Reservoir Engineering Stanford University, Stanford, California, February 13-15, 2017

Deng H, Ellis BR, Peters CA, et al (2013) Modifications of Carbonate Fracture Hydrodynamic Properties by CO_2 -Acidified Brine Flow. Energy Fuels 27:4221–4231. https://doi.org/10.1021/ef302041s

Fang Y, Elsworth D, Wang C, et al (2017) Frictional stability-permeability relationships for fractures in shales. Journal of Geophysical Research: Solid Earth 122:1760–1776

Fu P, Morris J (2020) Interpreting EGS Collab Exp. 1 downhole camera survey results

Fu P, Schoenball M, Morris J, et al (2019) Microseismic Signatures of Hydraulic Fracturing: A Preliminary Interpretation of Intermediate-Scale Data from the EGS Collab Experiment. Proceedings, 44th Workshop on Geothermal Reservoir Engineering Stanford University, Stanford, California, February 11-13, 2019

Ishibashi T, Watanabe N, Hirano N, et al (2012) Upgrading of Aperture Model Based on Surface Geometry of Natural Fracture for Evaluating Channeling Flow. GRC Transactions 36:

Ito T, Zoback MD (2000) Fracture permeability and in situ stress to 7 km depth in the KTB scientific drillhole. Geophysical Research Letters 27:1045–1048. https://doi.org/10.1029/1999GL011068

Javadi M, Sharifzadeh M, Shahriar K, Mitani Y (2014) Critical Reynolds number for nonlinear flow through rough-walled fractures: The role of shear processes. Water Resour Res 50:1789–1804. https://doi.org/10.1002/2013WR014610

Lee SH, Yeo IW, Lee K, Detwiler RL (2015) Tail shortening with developing eddies in a rough-walled rock fracture. Geophysical Research Letters 42:6340–6347. https://doi.org/10.1002/2015GL065116

Liu Y, Sharma MM (2005) Effect of Fracture Width and Fluid Rheology on Proppant Settling and Retardation: An Experimental Study. Society of Petroleum Engineers, Dallas, Texas, U.S.A., 9–12 October 2005

Okoroafor ER, Horne RN (2021) The Impact of Fracture Roughness on the Thermal Performance of Enhanced Geothermal Reservoirs. PhD Thesis, Energy Resources Engineering Department, Stanford University

Shaheed R, Mohammadian A, Kheirkhah Gildeh H (2019) A comparison of standard k–ε and realizable k–ε turbulence models in curved and confluent channels. Environ Fluid Mech 19:543–568. https://doi.org/10.1007/s10652-018-9637-1

Thomas R (1981) Characterization of surface roughness. Precision Engineering 3:97–104

Tse R, Cruden DM (1979) Estimating Joint Roughness Coefficients. Int J Rock Mech Min Sci & Geomech 16:303–307

Wang G, Mitchell TM, Meredith PG, et al (2016) Influence of gouge thickness and grain size on permeability of macrofractured basalt. JGR Solid Earth 121:8472–8487. https://doi.org/10.1002/2016JB013363

Xiao F, Shang J, Wanniarachchi A, Zhao Z (2021) Assessing fluid flow in rough rock fractures based on machine learning and electrical circuit model. Journal of Petroleum Science and Engineering 206:109126. https://doi.org/10.1016/j.petrol.2021.109126

Xiong F, Jiang Q, Ye Z, Zhang X (2018) Nonlinear flow behavior through rough-walled rock fractures: The effect of contact area. Computers and Geotechnics 102:179–195. https://doi.org/10.1016/j.compgeo.2018.06.006

Yang X, Tartakovsky DM, Horne RN (2023) Fracture Characterization by Temperature Log Interpretation Based on Machine Learning. Geothermal Resources Council Transactions 47:

Zou L, Jing L, Cvetkovic V (2017) Modeling of Solute Transport in a 3D Rough-Walled Fracture–Matrix System. Transp Porous Med 116:1005–1029. https://doi.org/10.1007/s11242-016-0810-z